

# Odd-One-Out: Anomaly Detection by Comparing with Neighbors

Ankan Bhunia Changjian Li Hakan Bilen  
University of Edinburgh

[github.com/VICO-UoE/OddOneOutAD](https://github.com/VICO-UoE/OddOneOutAD)

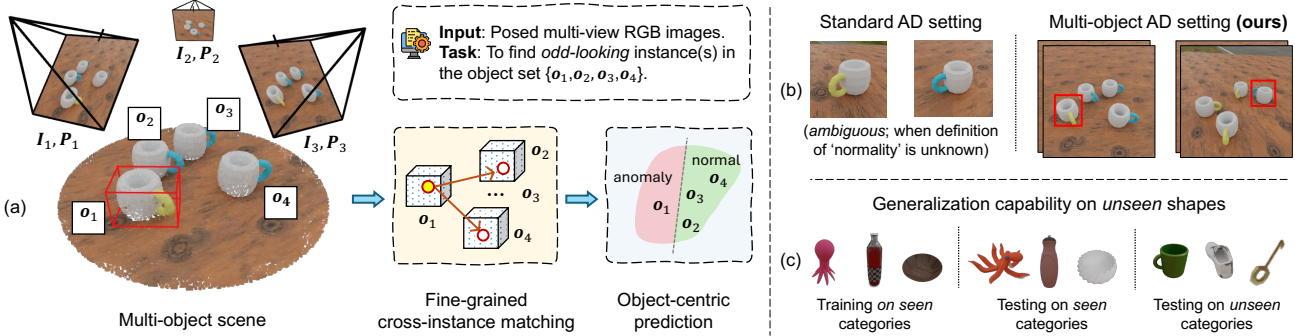


Figure 1. (a) We propose a new anomaly detection task focused on identifying ‘odd-looking’ objects relative to other instances within a scene. Inspired by real-world quality control in production environments, this task aims to detect subtle variations in geometry and texture, including defects like cracks and fractures, in a group of manufactured samples. (b) Our setting is scene-specific, requiring a comparison of object instances within the input scene, unlike the standard AD setting, which takes only a single object as input. (c) Our matching-based paradigm enables cross-category performance.

## Abstract

This paper introduces a novel anomaly detection (AD) problem that focuses on identifying ‘odd-looking’ objects relative to the other instances in a given scene. In contrast to the traditional AD benchmarks, anomalies in our task are scene-specific, defined by the regular instances that make up the majority. Since object instances may be only partly visible from a single viewpoint, our setting employs multiple views of each scene as input. To provide a testbed for future research in this task, we introduce two benchmarks, *ToysAD-8K* and *PartsAD-15K*. We propose a novel method that constructs 3D object-centric representations from multiple 2D views for each instance and detects the anomalous ones through a cross-instance comparison. We rigorously analyze our method quantitatively and qualitatively on the presented benchmarks. The datasets, source code, and models will be made available upon publication.

## 1. Introduction

Anomaly detection (AD) [10, 29] aims to detect patterns that deviate from expected behavior. In standard AD benchmark for computer vision, anomalies may arise from high-level

factors such as introduction of an object instance from an unseen category [2, 9, 31] or low-level ones such as defects and variations in the normal object shape and texture [6, 8, 13]. In these benchmarks, AD methods analyze each object individually, ignoring relationships between objects in the same scene or contextual factors. However, in many real-world scenarios, ‘normality’ can be conditional. For instance, in a production line for blue-handled coffee cups, a yellow handle is anomalous, and in a production line for yellow-handled coffee cups, a blue handle is anomalous (see Fig. 1(b)). This context dependent normality cannot be addressed by methods assuming a fixed standard of normality.

Inspired by real-world visual inspection, we introduce a new AD problem with two new benchmarks and a novel solution. In our setup (see Fig. 1(a)), each image contains a scene with multiple instances of the same object (e.g., coffee cup) including either all normal, or a mix of normal and anomalous instances. Since defining exact shape and appearance specifications on paper is often impractical, we assume each scene has multiple normal instances together providing a scene-specific reference for ‘normality’. Our objective is to detect anomalous instances in a scene and to generalize to previously unseen scenes including unseen objects and layouts. Unlike existing benchmarks, this task often requires

a holistic understanding of the scene by comparing instances with each other with the exception of few anomalies such as cracks and misaligned parts that can be identified by inspecting individual instances. Additionally, since performing AD from a single view can be ambiguous due to self-occlusion and occlusion between the instances, we provide multiple views of the scene to cover its entire relevant extent unlike existing benchmarks with single-view inputs (see Fig. 1(a)).

The proposed problem presents several challenges requiring the following key capabilities: i) achieving 3D understanding of the scene and view registration from multiple camera viewpoints without groundtruth 3D knowledge while handling occlusions, ii) aligning and comparing object instances without their pose information during training and testing, iii) learning representations that generalize to unseen object instances from seen or unseen categories at test time.

To tackle these challenges, we introduce a novel method that takes as input multiple views of the same scene, projects them into a 3D voxel grid, generates a 3D object-centric representation for each instance, and predicts their labels by cross-correlating instances using an efficient attention mechanism. We utilize advances in differentiable rendering [26] and self-supervised learning [28] to supervise 3D representation learning. Specifically, we render the voxel representations for multiple viewpoints and match them with the given 2D views to produce geometrically consistent features. Additionally, we encourage our model to learn part-aware 3D representations by distilling features from 2D self-supervised model DINOv2 [28], enhancing the correspondence matching across instances and their alignment. Finally, since there is no prior benchmark for this task, we propose two new benchmarks – *ToysAD-8K* and *PartsAD-15K*, which include common objects categories as well as mechanical parts respectively to facilitate further research. Our method significantly outperforms baselines that do not compare instances with each other, and we rigorously analyze various aspects of our model and benchmarks.

## 2. Related Work

**AD benchmarks.** A key challenge in AD research is the scarcity of large datasets containing realistic anomalies. Earlier works [9, 31] focusing on high-level semantic anomalies often use existing classification datasets by treating a subset of classes as anomalies and the remainder as normal. There also exist several datasets containing real-world anomaly instances. For example, MVTEC-AD [5] includes industrial objects with various defects like scratches, dents, and contaminations, Carrera *et al.* [8] presents various defects in nanofibrous material, and VisA [52] comprises complex industrial objects such as PCBs, as well as simpler objects like capsules and cashews, spanning a total of 12 categories. These datasets assume that objects are pose-aligned, and both normal images and their anomaly counterparts have

the same pose. Zhou *et al.* [51] propose a pose-agnostic framework by introducing the PAD dataset, which comprises images of 20 LEGO bricks of animal toys from diverse viewpoints/poses. Unlike the works discussed above, we focus on AD in multi-object multi-view scene environments, where anomalies are predicted by assessing their mutual similarity with other objects in the scene. The proposed setting enables our framework to work seamlessly on novel object instances without requiring further training.

**Few-shot AD.** There are some works [15, 19, 44, 46] aiming to detect anomalies from a small number of normal samples as support images. In our setting, the concept of normality in each image is also learned from a few instances only. However, unlike them, the concept of normality is scene-specific, and our method can generalize to previously unseen instances without requiring any modification by learning from a support set. In addition, our setting involves multi-object multi-view data samples as input, unlike the single-object single-view in theirs.

**Multi-view 3D vision.** Multi-view 3D detection [32, 35, 43, 45] is a related problem that aims to predict the locations and classes of objects in 3D space, given multi-view images of a scene along with their corresponding camera poses as input. Most existing works first project 2D image features onto a 3D voxel grid, followed by a detection head [7, 24, 47] that outputs the final 3D bounding boxes and class labels. While our task can be naively solved by treating it as a 3D object detection problem with anomaly and normal as the two possible classes, this approach has limited ability to perform effective comparisons with other instances in the scene, which is required for fine-grained AD. We compare our method to a 3D object detection technique in Sec. 4. Another related area involves taking multi-view images as input and training a feedforward model for 3D volume-based reconstruction [27, 37, 49] and novel view synthesis [12, 20, 39, 41, 48]. Similarly, in this work, we focus on learning a feedforward model in a multi-object scene environment using sparse multi-view images but for AD.

**Leveraging large-scale models.** Large-scale pretraining on image datasets has shown impressive generalization capabilities on various tasks [21, 28, 30]. Previous works [3, 50] demonstrate that features extracted from DINOv2 [28] serve as effective dense visual descriptors with localized semantic information for dense correspondence estimation tasks. Some recent works [22, 40] use feature distillation techniques to leverage 2D foundation vision models for 3D tasks. Inspired by these works, we utilize DINOv2 to distill its dense semantic knowledge into our 3D network enabling our network to infer robust local correspondences, which aids in fine-grained object matching.

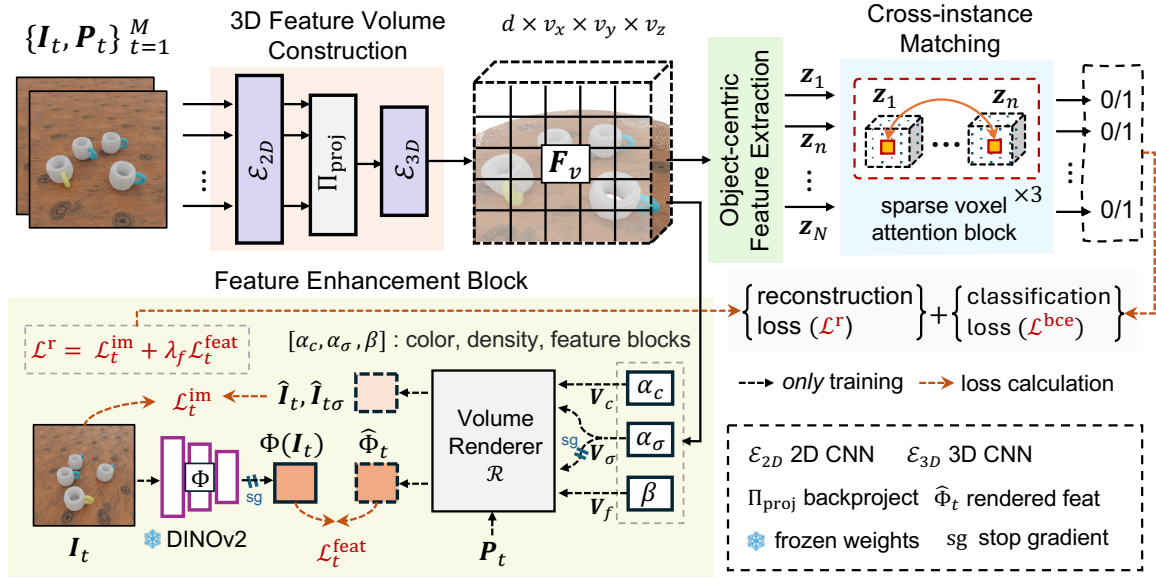


Figure 2. Overview of our framework. We extract features from a sequence of input views using a 2D CNN and back-project them into a 3D volume, which is then refined with a 3D CNN, resulting in  $F_v$ . Next, we extract object-centric feature volumes  $\{z_n\}_{n=1}^N$ , which are fed into the cross-instance matching module to learn correlations among objects using sparse voxel attention. To improve the 3D representation of the scene, we distill the knowledge of a 2D vision model namely DINOv2, and integrate the learned knowledge into our 3D network via differentiable rendering. This aids in obtaining a part-aware and geometrically consistent 3D feature representation.

### 3. Method

Consider a scene containing  $N$  instances  $\{o_n\}_{n=1}^N$  of the same rigid object where their poses are unknown. The goal is to identify anomalies in the group of objects by assessing their mutual similarity. An observation in our setting consists of  $M$ -view  $H \times W$  dimensional RGB images  $\mathcal{I} = \{I_t\}_{t=1}^M$ , and their corresponding camera projection matrices  $\mathcal{P} = \{P_t\}_{t=1}^M$  where  $P_t = K[R_t|T_t]$ , with intrinsic  $K_t$ , rotation  $R_t$  and translation  $T_t$  matrices. We set  $M$  to 5, forming sparse-view inputs in our experiments. Our goal is to learn a mapping  $\psi$  from the multi-view images to object-centric anomaly labels  $y_n \in \{0, 1\}$  and its corresponding 3D bounding box  $b_n$ , defined as:

$$\psi : \{(I_t, P_t)\}_{t=1}^M \mapsto \{(y_n, b_n)\}_{n=1}^N. \quad (1)$$

Note that labels  $y_n$  are defined relative to other objects in the scene. For example, consider a group of three coffee cups, of which two have *yellow* handles, and one has a *blue* handle. In this example, the latter cup is considered an anomaly.

Our pipeline, illustrated in Fig. 2, is comprised of four main components: First, the *3D feature volume construction* module (Sec. 3.1) encodes each view image and projects it to 3D, forming a fused 3D feature volume. Second, the *feature enhancement* block (Sec. 3.2), employed *only* during training, facilitates the learning of a part-aware and geometrically consistent 3D space through differentiable rendering and feature distillation. Third, the *object-centric feature extraction* module (Sec. 3.3) locates each object in the scene and rep-

resents it with a feature volume. Finally, the *cross-instance matching* module (Sec. 3.4) efficiently compares all similar object regions using a sparse voxel attention mechanism and predicts instance anomalous labels and 3D coordinates. Next, we elaborate on details.

#### 3.1. 3D Feature Volume Construction

In our first module, we obtain a 3D feature volume representation given multi-view images as input. Specifically, we first extract 2D features  $F_t = \mathcal{E}_{2D}(I_t) \in \mathbb{R}^{d \times h \times w}$  for each input view using a shared CNN encoder  $\mathcal{E}_{2D}$ , where  $d$  is the feature dimension. These 2D features are then projected into 3D voxel space as follows:

$$F_v = \mathcal{E}_{3D}(\text{agg}(\{\Pi_{\text{proj}}(F_t, P_t)\}_{t=1}^M)), \quad (2)$$

where  $\Pi_{\text{proj}}$  back-projects each view feature  $F_t$  using known camera intrinsic and extrinsic parameters, generating 3D feature volumes of size  $d \times v_x \times v_y \times v_z$ . These feature volumes are aggregated over all input views using an average operation as in [27, 37]. Finally, a 3D CNN-based network  $\mathcal{E}_{3D}$  is employed to refine the aggregated feature volume, resulting in a final voxel representation  $F_v$  of size  $d \times v_x \times v_y \times v_z$ , which is further fed into the feature enhancement block, described next, to obtain a part-aware and geometrically consistent 3D representation.

#### 3.2. Feature Enhancement Block

We use volume rendering [26] to reconstruct the geometry and appearance of the scene. We implement the rendering

operation as in [20], where for each 3D query point on a ray, we retrieve its corresponding features by bilinearly interpolating between the neighboring voxel grids. Specifically, we first apply a two-layered  $1 \times 1 \times 1$  convolution block, *i.e.*,  $\alpha_c$  and  $\alpha_\sigma$  respectively, to obtain color and density volumes denoted as  $(\mathbf{V}_c, \mathbf{V}_\sigma)$ . Then, the pixel-wise color and density maps are composed by integrating along a camera ray using volume renderer  $\mathcal{R}$ . Following this, we compute the L2 image reconstruction loss  $\mathcal{L}_t^{\text{im}}$ . Formally, the image rendering and its corresponding loss function for a single viewpoint  $\mathbf{P}_t$  are shown below:

$$\mathcal{L}_t^{\text{im}} = \|\mathbf{I}_t - \hat{\mathbf{I}}_t\|^2 + \|\mathbf{I}_{t\sigma} - \hat{\mathbf{I}}_{t\sigma}\|^2, \quad (3)$$

where  $[\hat{\mathbf{I}}_t, \hat{\mathbf{I}}_{t\sigma}] = \mathcal{R}([\mathbf{V}_c, \mathbf{V}_\sigma], \mathbf{P}_t)$ ,  $\hat{\mathbf{I}}_t$  and  $\hat{\mathbf{I}}_{t\sigma}$  are the rendered image and mask.

Moreover, we improve the 3D voxel representation  $\mathbf{F}_v$  by reconstructing neural features in addition to geometry and appearance. We supervise the feature reconstruction by a pretrained 2D image encoder  $\Phi$  as a teacher network. We choose DINOv2 [28] as the teacher network due to its excellent ability to capture various object geometries and correspondences. To this end, we use a projector function  $\beta$ , instantiated as a four-layered  $1 \times 1 \times 1$  convolution block that projects  $\mathbf{F}_v$  to a *neural feature field*  $\mathbf{V}_f$ , changing the channel dimension from  $d$  to  $d_f$ . Similar to color rendering, taking  $\mathbf{V}_f$  and  $\mathbf{V}_\sigma$  as input, we generate rendered features  $\hat{\Phi}_t$  of size  $d_f \times h_f \times w_f$  at a given viewpoint using volume renderer  $\mathcal{R}$ , and minimize the difference between the rendered features and the teacher’s features  $\Phi(\mathbf{I}_t)$ . We choose cosine distance as our feature loss ( $\mathcal{L}_t^{\text{feat}}$ ), which we find easier to optimize compared to the standard L2 loss. We do not allow the gradients to follow through the density in the rendering of features  $\hat{\Phi}_t$ , as the teacher’s features are not fully multi-view consistent [3], which could harm the quality of reconstructed geometry. The final reconstruction loss is the sum of all image and feature reconstruction losses:

$$\mathcal{L}^r = \sum_{t=1}^M (\mathcal{L}_t^{\text{im}} + \mathcal{L}_t^{\text{feat}}). \quad (4)$$

The key benefits of reconstructing DINOv2 features are twofold. First, distilling features from general-purpose feature extractors pretrained on large external datasets incorporates open-world knowledge into the 3D representation. This enables our model to perform significantly better on unseen object instances or even on novel categories, as demonstrated in the experiments. Second, the distillation through rendering enforces *consistent* 3D scene representation, leading to very similar features for the same object geometries. This enables the model to infer robust local *correspondences* (see Fig. 6), which aids in fine-grained object matching.

### 3.3. Object-centric Feature Extraction

Having the enhanced 3D feature volume representation, we aim to localize each object instance in the scene and represent each with a 3D feature volume such that the instances can be compared to each other in the next step. To this end, we use the predicted density volume  $\mathbf{V}_\sigma$ , obtained in Sec. 3.2, to extract a coarse point-cloud structure of the scene by applying a threshold to  $\mathbf{V}_\sigma$ . Then, we employ DBScan [17], a density-based clustering method to segment the foreground objects in the point cloud. This produces bounding box regions  $\{\mathbf{b}_n\}_{n=1}^N$  corresponding to the objects in the scene. Finally, we apply RoI pooling [14] on the voxel representation  $\mathbf{F}_v$  to extract object-centric feature volumes  $\{\mathbf{z}_n\}_{n=1}^N$ , each with a size of  $d \times 8 \times 8 \times 8$ . Note that we do not require ground truth box coordinates during training. Next, we pass them to the cross-instance matching module for fine-grained comparison.

### 3.4. Cross-instance Matching

Our task requires comparing object instances with each other, which further demands geometric alignment for each pair. Since the relative pose of each instance with respect to the camera is unknown, we avoid explicit alignment and instead focus on finding local matches between them. To this end, for a given pair of object instances ( $m$  and  $n$ ), we compute the most similar local features between their feature volumes ( $\mathbf{z}_n$  and  $\mathbf{z}_m$ ) respectively:

$$\mathcal{C}_k^{nm}[i] = \text{top}_k[\beta(\mathbf{z}_n[i])^T \beta(\mathbf{z}_m[\cdot])], \quad (5)$$

where we denote the operation as  $\mathcal{C}_k^{nm}$ , which returns top- $k$  most relevant feature locations in  $\mathbf{z}_m$  for the  $i$ -th voxel location in  $\mathbf{z}_n$ . This is achieved by first projecting each voxel feature utilizing the projector function  $\beta$  (described in Sec. 3.2 and then computing their voxel-level pairwise similarity followed by a  $\text{top}_k$  operation. We use  $\mathcal{C}_k^{nm}$  to perform sparse attention-based comparisons between multiple object volumes, as described next.

The query, key, and value embeddings are calculated using linear projections as:

$$\begin{aligned} \mathbf{Q}_n[i] &= \mathbf{W}^Q \mathbf{z}_n[i], & \mathbf{K}_n[i] &= \mathbf{W}^K \mathbf{z}_n[i], \\ \mathbf{V}_n[i] &= \mathbf{W}^V \mathbf{z}_n[i], \end{aligned} \quad (6)$$

where the weights  $\mathbf{W}^Q$ ,  $\mathbf{W}^K$  and  $\mathbf{W}^V$  are shared across all objects. Then, the attention is calculated as:

$$\bar{\mathbf{z}}_n[i] = \sum_{\substack{m=1 \\ m \neq n}}^N \sum_{j \in \mathcal{C}_k^{nm}[i]} \text{softmax} \left( \frac{\mathbf{Q}_n[i] \mathbf{K}_m[j]}{\sqrt{d}} \right) \mathbf{V}_m[j]. \quad (7)$$

Unlike the vanilla self-attention module in standard transformers [16] that uses all tokens for the attention computation, which is inefficient for our task and may introduce



noisy interactions with irrelevant features, potentially degrading performance. To overcome this, we compute the sparse voxel attention only among geometrically corresponding voxel locations using  $C_k^{nm}$ .

Next, the updated feature volume  $\bar{z}_n$  is passed through 3D CNN blocks to downsample by a factor of 1/8, which is finally reshaped into a vector and fed to a 2-layer MLP outputting the final prediction  $\hat{y}_n$ . The classification loss is calculated as:

$$\mathcal{L}^{\text{bce}} = \sum_{n=1}^N \ell_{\text{bce}}(\hat{y}_n, y_n), \quad (8)$$

where  $\ell_{\text{bce}}$  is the binary cross-entropy loss function. The total training loss of our framework is  $\mathcal{L} = \mathcal{L}^{\text{bce}} + \mathcal{L}^r$ .

## 4. Experiments

### 4.1. Datasets

We have proposed two new benchmarks for multi-object AD: *ToysAD-8K* and *PartsAD-15K*. *ToysAD-8K* consists of real-world objects from *multiple* categories that enables to evaluate our model’s ability to generalize to unseen object categories. *PartsAD-15K* comprises a more diverse collection of mechanical object parts with arbitrary shapes, thus being free from any class-level inductive biases (*e.g.*, a sheep with three legs are easy to be recognized as anomaly without comparison) of common objects. Both datasets include a wide range of fine-grained anomaly instances motivated by real-world applications in inspection and quality control. Scenes are generated with diverse backgrounds, illuminations, and camera viewpoints using photo-realistic ray tracing [38]. Next, we discuss the data generation for both datasets.

**ToysAD-8K.** We start with a subset of 1050 shapes from the Toys4K dataset [36], covering a wide range of objects across 51 categories. Anomalies are automatically generated for each 3D shape by applying various deformations to both the geometry and texture. These include realistic cracks and fractures using [34], applying random geometric deformations [38] like bumps, bends, and twists, as well as randomly translating, rotating, and swapping materials in different parts of the shapes. This process results in a total of 2345 anomaly shapes.

To generate each scene, we randomly select a set of objects consisting of both the normal and anomalous variants of the same instance. Most scenes contain more normal objects than anomalies and few scenes have no anomalous instances. The resting poses for the objects are generated using rigid body simulation [4] by dropping the object to the floor. Objects are scaled and placed randomly in the scene while avoiding collisions. We generated a total of 8K scenes. Each scene consists of 3-6 objects rendered in 20 views. For the training set, we randomly select 5K scenes

from 39 categories. We build two disjoint test sets. The first one (*seen*) contains 1K scenes from the seen categories but with unseen object instances. The second one (*unseen*) contains 2K scenes from the rest of the 12 novel categories.

**PartsAD-15K.** We use a subset of the ABC dataset [23] that consists of 4200 shapes. Anomalies are generated following the same strategy outlined above. Additionally, for each shape, we sample geometrically close instances from the dataset and assign them as anomalies to use in the same scene. This results in high-quality anomalies that closely resemble their normal counterparts in overall geometry but differ in subtle shape variations, making them anomalous in the context of the normal ones. In total, we generate 10,203 anomaly shapes and create 15K scenes, each consisting of 3 to 12 objects rendered from 20 different viewpoints. The dataset is split into a 12K training set and the remaining 3K scenes (unseen shapes) as the test set.

**Anomaly generation and checking.** Our anomaly generation process is fully automated with several quality checks to ensure the anomalies are realistic. For example, if a part detaches from the main body during positional or rotational deformations, the anomaly is discarded and regenerated with adjusted parameters. Similarly, if removing a part makes the shape disconnected (*e.g.*, teddy bear with a floating hand after removing an arm), we discard the anomaly and try a different part. For fracture anomalies, if a particular fracture removes more than 90% or less than 10% of an object, it is rejected and regenerated. We also ensure that the anomalous region of an object is visible from at least one viewpoint.

### 4.2. Implementation details

We use a ResNet50-FPN [25] as the 2D encoder backbone and a four-scale encoder-decoder-based 3D CNN [27] as the 3D backbone. For input, we use  $M=5$  views, each with a resolution of  $256 \times 256$ , though our model can accept a different  $M$  during inference. During training, we use  $2M$  views, divided into two sets of  $M$  views. One set is used to build the neural feature volume, while the other set’s camera views are used to render the results, and vice versa.

The 3D volume  $F_v$  contains  $96 \times 96 \times 16$  voxels with a voxel size of  $4cm$ . We sample 128 points per ray for rendering, and the rendered features ( $\hat{\Phi}_t$ ) have a spatial dimension of  $32 \times 32$  (*i.e.*,  $h_f \times w_f$ ). The ground truth segmentation mask of the input image ( $I_{t\sigma}$  in Eq. (3)) is only used during training. The threshold applied to the density volume  $V_\sigma$  is set to be 0.2 and the DBScan algorithm is run with its default parameters.

We resize the teacher’s (DINOv2) features to the same spatial dimension for loss computation. These features are precomputed for all scenes using the publicly available weights, which are not updated during distillation. These DINOv2 features are then reduced to  $d_f=128$  channel dimension using PCA before distillation. We employ three

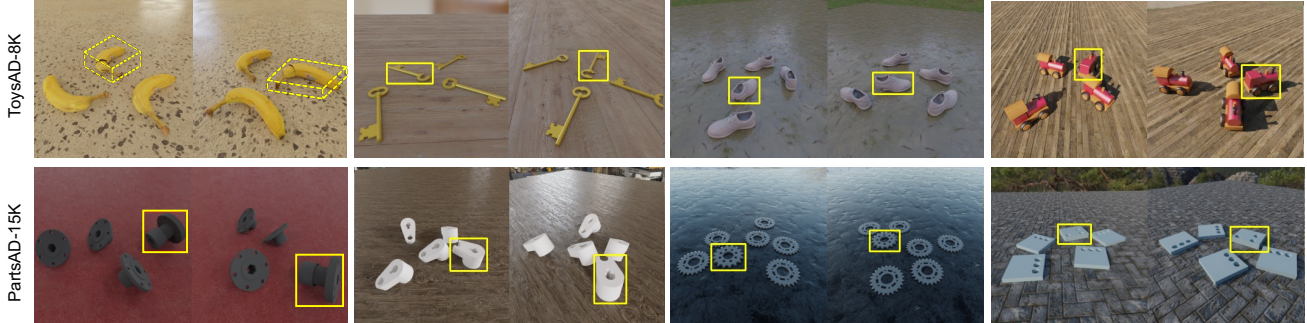


Figure 3. AD qualitative results on the *unseen* test categories of ToysAD-8K (top row) and the test set of PartsAD-15K (bottom row) using our proposed framework. Due to limited space, two views are shown per scene. The model prediction is shown with a yellow bounding box: a 3D box for the first example (banana) and a projected box for the others for simplicity. Our model successfully predicts the correct object in all cases shown above.

Table 1. **Quantitative results.** We compare our method to three related works in two datasets and report the results in terms of anomaly detection AUC and accuracy.

Datasets	Recon-Recog		ImVoxelNet [32]		DETR3D [43]		Ours	
	AUC	Accuracy	AUC	Accuracy	AUC	Accuracy	AUC	Accuracy
ToysAD-8K-Seen	73.45	60.48	78.13	65.55	79.16	67.37	<b>91.78</b>	<b>83.21</b>
ToysAD-8K-Unseen	72.86	58.12	73.19	60.12	74.60	62.98	<b>89.15</b>	<b>81.57</b>
PartsAD-15K	72.78	61.34	72.80	64.34	74.49	65.11	<b>86.12</b>	<b>79.68</b>

sparse voxel attention blocks, and each applies 8-headed attention with  $k=20$ . The network is first pretrained for 50 epochs with only the reconstruction loss to build a reliable initialized 3D feature volume, then trained end-to-end with both the reconstruction and the binary classification losses for another 50 epochs. The batch size is 4, and we use the Adam optimizer with a learning rate  $2 \times 10^{-5}$ . The run-time of our method is 65ms on a single A40 GPU for a typical scene with 5 views as input.

### 4.3. Baseline Comparisons

We evaluate the anomaly classification results using two metrics – the area under the ROC curve (AUC) and accuracy. A prediction is considered correct if the bounding box IoU is greater than 0.5 and the anomaly classification is correct. We do not use a separate localization metric since our bounding box estimations are highly accurate. These metrics are calculated object-wise and then averaged across all test scenes.

Since no prior work exists for this task, we compare our method with two relevant competitive baselines: a reconstruction-based baseline and two multi-view 3D object detection methods in Tab. 1. For the reconstruction-based baseline, we first employ COLMAP [33] to generate a point cloud reconstruction of the multi-object scene environment. We use default dense reconstruction parameters but utilize the provided ground truth camera matrices. Given

that 5 views are insufficient, we use a total of 20 views to reconstruct the scene. We extract point clouds from the reconstructed scenes for each object, and train a Siamese-style network to obtain their pairwise similarity. We use DGCNN [42] (pretrained on ShapeNet [11]) as the point cloud feature extractor and the triplet loss [18] to supervise the network. A voting strategy is then applied to aggregate the pairwise distances of all objects in the scene and classify the objects. However, this method’s performance is highly sensitive to the reconstruction quality, resulting in poor performance on both datasets.

Next, we adapt two multi-view object detection frameworks, ImVoxelNet [32] and DETR3D [43], to locate and classify each object in the scene as either anomalous or normal. ImVoxelNet constructs a voxel representation using a 2D-3D projection similar to ours, followed by a 3D detection head [24] for the final prediction. DETR3D, a transformer-based design, uses the set prediction loss [7] for end-to-end detection without non-maximum suppression. Both models are trained on our datasets and their performance is evaluated object-wise based on the output of the classification head, similar to ours. After examining the qualitative results (see supplementary), we observe that although both methods perform well for large cracks or fractures, they struggle when intra-group comparison is necessary. This is because they tend to memorize certain anomaly types and fail to capture the cross-object relations in the scene.

Our method significantly outperforms all baselines on both datasets (see Tab. 1). This highlights the effectiveness of our architecture, which is designed to match corresponding regions across objects. Notably, our model exhibits a smaller performance drop on the *unseen* set, thanks to the robust 3D representation that generalizes to novel categories. Qualitative results of our method are shown in Fig. 3

#### 4.4. Ablations and Model Analysis

In this section, we present an ablation study of our model, analyze its robustness, and evaluate its performance on real scenes. Unless stated otherwise, all experiments are conducted on the ToysAD-8K *unseen* set using 5 input views.

**Ablation of architecture design.** We evaluate the main components of our model through an ablation study and report the results in Tab. 2. All variants include the 3D feature fusion module and are optimized at least for the image reconstruction loss, which is essential for constructing scene geometry. Variant A directly maps object-centric features to their binary labels using an MLP without comparing them. In contrast, variant B applies standard attention layers to the object-centric features to learn cross-object correlations. Despite the attention layers, B only shows a slight improvement (+2.1% AUC) over A.

Table 2. Ablation Results on ToysAD-8K.

Variants	AUC	Accuracy
A: baseline	79.13	66.78
B: A + vanilla attention	81.24	68.20
C: B + feature distillation	87.05	79.56
Final: C + sparse voxel attention	<b>89.15</b>	<b>81.57</b>

We then introduce DINOv2 feature distillation (variant C), which significantly improves performance by 5.8% AUC and 11.3% accuracy. This demonstrates the importance of the part-aware 3D representation and correspondences for our task (see Fig. 6). Our final design achieves further performance gain by using sparse voxel attention, which focuses on the top- $k$  most relevant features. This leverages robust correspondences learned through DINOv2 feature distillation, effectively eliminating noisy correlations and directing attention solely to corresponding object regions.

**Robustness.** Our method demonstrates robustness to occlusions by effectively utilizing input from multiple viewpoints. As shown in Fig. 4, our model accurately identifies the anomalous region even when parts of the object are occluded in some views. In Fig. 5 (left), we show how well our model can perform with varying numbers of input views during testing. Trained with 5 views, the model is evaluated using 1, 3, 5, 10, and 20 views. The results clearly show that our model performs well with only 3-5 views, while additional views further enhance the performance.



Figure 4. Resolving occlusion and 3D ambiguity using multi-view images. The anomaly ‘sheep’ in *top* has a missing tail (only visible in the 2nd view due to occlusion), and the ‘hammer’ handle in *bottom* is bent (only apparent from the 2nd view-angle due to 3D ambiguities).

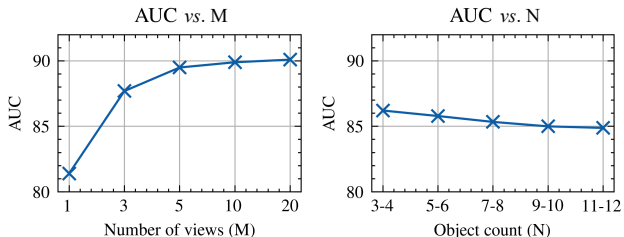


Figure 5. Impact of the number of views (left) and object count (right) on model performance.

We analyze the impact of object count on model performance (see Fig. 5 (right)) using the PartsAD-15K dataset. As the number of objects in a scene increases, occlusion and lower resolution for individual objects typically occur. However, the performance drop between the two extremes is minimal ( $< 1.5\%$  AUC) as shown in the figure. We also assess the model’s ability to generalize to scenes with more objects than it encountered during training. To this end, we trained our model on scenes with 3-7 objects (AUC: 86.75) and tested on two sets: one with 3-7 objects (AUC: 86.75) and another with 8-12 objects (AUC: 85.10). These results demonstrate our model’s adaptability to varying object counts.

In another experiment, we assess our model’s performances when varying the ratio of normal to anomalous instances during testing as shown in Fig. 8. We create five scenes (a-e) by using two geometrically similar objects  $ob1$  and  $ob2$ , and gradually introduce more instances of  $ob1$  (1 to 5 respectively) while maintaining a total of six objects. For example, in scene (a),  $ob1$  appears only once, making it an anomaly. Similarly, in scene (e),  $ob2$  appears only once, hence considered an anomaly. We utilize a consistent background across all scenes to ensure uniformity. As shown in the figure, our model correctly classifies the anomalies in



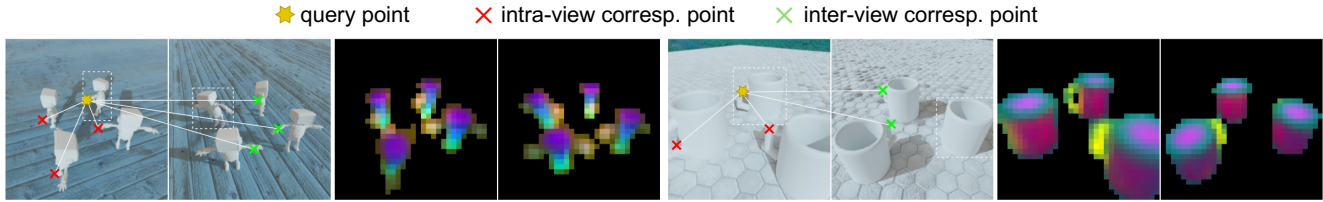


Figure 6. Correspondences are obtained in 3D using the *neural feature field*  $V_f$  and projected onto 2D views via camera matrices for visualization. The feature field is rendered at respective viewpoints, with the first 3 PCA components mapped to different color channels.

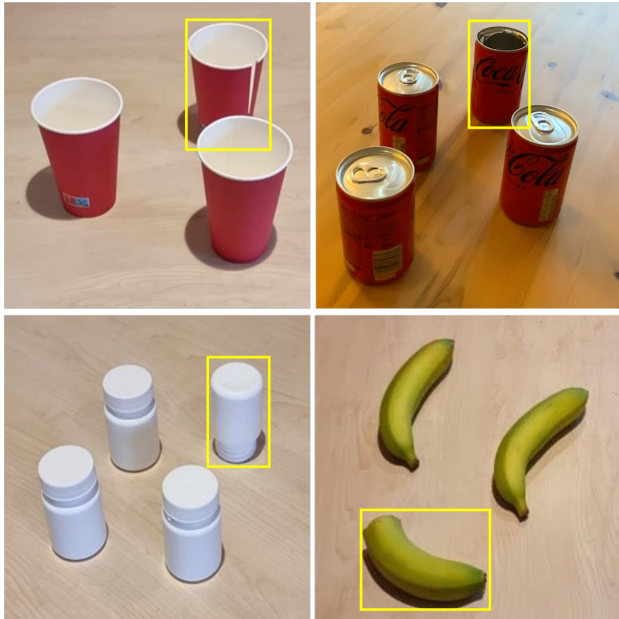


Figure 7. Four real-world scenes are tested using our method and it can successfully detect all anomalous instances. Five views are used for testing, but only one view per scene is shown.

each scene. We note scene (c) presents an ambiguous case, where both objects appear in equal numbers. Despite this, our model is able to separate the two groups.

**Real world testing.** We apply our model, trained on the synthetic dataset, to a small set of real test scenes (a tabletop with three cups, four coca-cola cans, four medicine bottles, or three bananas). Each scene is captured in an indoor environment with adequate lighting using a 3D scanning software [1]. We obtain a set of input views of the scenes with globally optimized camera intrinsic and extrinsic parameters, which are then fed into our trained model. The results are shown in Fig. 7. Our model is able to correctly distinguish the anomaly objects in all four scenes.

**Limitations.** Our benchmark and model have a few limitations. First, this work focuses on a specific set of anomalies common in manufacturing scenarios, potentially overlooking other types of anomalies found in different applications. Due to the high cost and difficulty of obtaining real damaged objects, our dataset primarily uses shapes of synthetic ob-

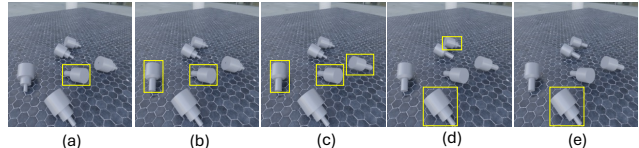


Figure 8. We create five scenes (a-e) with two similar objects, varying their counts per scene while maintaining a constant total. Our model correctly identifies minorities as anomalies in all cases except (c), where an equal number of objects creates ambiguity. Our model still selects one group. The yellow box indicates the predicted anomaly object.

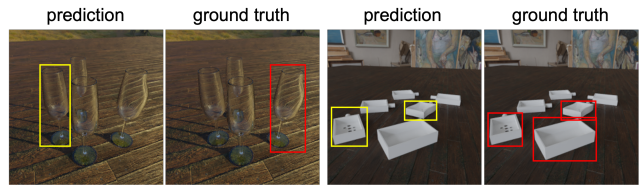


Figure 9. Failure cases. We use yellow box for our model’s prediction and red box for the ground truth. In the first example, our model incorrectly predicts an anomaly, while in the second, it correctly identifies two objects but misses the third anomaly.

jects. Additionally, our model assumes that object instances are rigid and does not handle articulations or deformations. It also assumes objects are not touching nor fully occluded in the scene. Furthermore, when a scene contains mostly anomalies, the lack of ‘normal’ data points for comparison (except in cases like fractures or cracks) can make detection more challenging. Lastly, during real-world scene testing, factors such as noisy camera poses and the gap between synthetic and real environments may degrade the performance. Fig. 9 shows some failure cases of our model.

## 5. Conclusion

In this paper, we have introduced a novel AD problem inspired by real-world applications along with two new benchmarks. The proposed task goes beyond the traditional AD setting and involves a cross study of objects in a scene from multiple camera viewpoints to identify the ‘odd-looking’ instances. We show that our model is robust to varying number of views and objects, and outperforms the baselines that do not consider cross-object correlations.



## References

- [1] Polycam. <https://github.com/PolyCam/polyform>. 8
- [2] Faruk Ahmed and Aaron Courville. Detecting semantic anomalies. In *AAAI*, 2020. 1
- [3] Mohamed El Banani, Amit Raj, Kevis-Kokitsi Maninis, Abhishek Kar, Yuanzhen Li, Michael Rubinstein, Deqing Sun, Leonidas Guibas, Justin Johnson, and Varun Jampani. Probing the 3d awareness of visual foundation models. In *CVPR*, 2024. 2, 4
- [4] David Baraff. Physically based modeling: Rigid body simulation. In *ACM SIGGRAPH*, 2001. 5
- [5] Paul Bergmann, Michael Fauser, David Sattlegger, and Carsten Steger. Mvtec ad—a comprehensive real-world dataset for unsupervised anomaly detection. In *CVPR*, 2019. 2
- [6] Paul Bergmann, Xin Jin, David Sattlegger, and Carsten Steger. The mvtec 3d-ad dataset for unsupervised 3d anomaly detection and localization. *arXiv preprint arXiv:2112.09045*, 2021. 1
- [7] Nicolas Carion, Francisco Massa, Gabriel Synnaeve, Nicolas Usunier, Alexander Kirillov, and Sergey Zagoruyko. End-to-end object detection with transformers. In *ECCV*, 2020. 2, 6
- [8] Diego Carrera, Fabio Manganini, Giacomo Boracchi, and Ettore Lanzarone. Defect detection in sem images of nanofibrous materials. In *IEEE Transactions on Industrial Informatics*, 2016. 1, 2
- [9] Raghavendra Chalapathy, Aditya Krishna Menon, and Sanjay Chawla. Anomaly detection using one-class neural networks. *arXiv preprint arXiv:1802.06360*, 2018. 1, 2
- [10] Varun Chandola, Arindam Banerjee, and Vipin Kumar. Anomaly detection: A survey. In *ACM Computing Surveys*, 2009. 1
- [11] Angel X Chang, Thomas Funkhouser, Leonidas Guibas, Pat Hanrahan, Qixing Huang, Zimo Li, Silvio Savarese, Manolis Savva, Shuran Song, Hao Su, et al. Shapenet: An information-rich 3d model repository. *arXiv preprint arXiv:1512.03012*, 2015. 6
- [12] Anpei Chen, Zexiang Xu, Fuqiang Zhao, Xiaoshuai Zhang, Fanbo Xiang, Jingyi Yu, and Hao Su. Mvsnerf: Fast generalizable radiance field reconstruction from multi-view stereo. In *ICCV*, 2021. 2
- [13] Lucas Deecke, Lukas Ruff, Robert A Vandermeulen, and Hakan Bilen. Transfer-based semantic anomaly detection. In *ICML*, 2021. 1
- [14] Jiajun Deng, Shaoshuai Shi, Peiwei Li, Wengang Zhou, Yanyong Zhang, and Houqiang Li. Voxel r-cnn: Towards high performance voxel-based 3d object detection. In *AAAI*, 2021. 4
- [15] Choubo Ding, Guansong Pang, and Chunhua Shen. Catching both gray and black swans: Open-set supervised anomaly detection. In *CVPR*, 2022. 2
- [16] Alexey Dosovitskiy, Lucas Beyer, Alexander Kolesnikov, Dirk Weissenborn, Xiaohua Zhai, Thomas Unterthiner, Mostafa Dehghani, Matthias Minderer, Georg Heigold, Sylvain Gelly, et al. An image is worth 16x16 words: Transformers for image recognition at scale. In *ICLR*, 2021. 4
- [17] Martin Ester, Hans-Peter Kriegel, Jörg Sander, and Xiaowei Xu. Density-based spatial clustering of applications with noise. In *ACM SIGKDD international conference on Knowledge discovery and data mining*, 1996. 4
- [18] Elad Hoffer and Nir Ailon. Deep metric learning using triplet network. In *Similarity-Based Pattern Recognition: Third International Workshop, SIMBAD*, 2015. 6
- [19] Chaoqin Huang, Haoyan Guan, Aofan Jiang, Ya Zhang, Michael Spratling, and Yan-Feng Wang. Registration based few-shot anomaly detection. In *ECCV*, 2022. 2
- [20] Hanwen Jiang, Zhenyu Jiang, Kristen Grauman, and Yuke Zhu. Few-view object reconstruction with unknown categories and camera poses. *arXiv preprint arXiv:2212.04492*, 2022. 2, 4
- [21] Alexander Kirillov, Eric Mintun, Nikhila Ravi, Hanzi Mao, Chloe Rolland, Laura Gustafson, Tete Xiao, Spencer Whitehead, Alexander C Berg, Wan-Yen Lo, et al. Segment anything. In *ICCV*, 2023. 2
- [22] Sosuke Kobayashi, Eiichi Matsumoto, and Vincent Sitzmann. Decomposing nerf for editing via feature field distillation. 2022. 2
- [23] Sebastian Koch, Albert Matveev, Zhongshi Jiang, Francis Williams, Alexey Artemov, Evgeny Burnaev, Marc Alexa, Denis Zorin, and Daniele Panozzo. Abc: A big cad model dataset for geometric deep learning. In *CVPR*, 2019. 5
- [24] Alex H Lang, Sourabh Vora, Holger Caesar, Lubing Zhou, Jiong Yang, and Oscar Beijbom. Pointpillars: Fast encoders for object detection from point clouds. In *CVPR*, 2019. 2, 6
- [25] Tsung-Yi Lin, Piotr Dollár, Ross Girshick, Kaiming He, Bharath Hariharan, and Serge Belongie. Feature pyramid networks for object detection. In *CVPR*, 2017. 5
- [26] Ben Mildenhall, Pratul P Srinivasan, Matthew Tancik, Jonathan T Barron, Ravi Ramamoorthi, and Ren Ng. Nerf: Representing scenes as neural radiance fields for view synthesis. In *Communications of the ACM*, 2021. 2, 3
- [27] Zak Murez, Tarrence Van As, James Bartolozzi, Ayan Sinha, Vijay Badrinarayanan, and Andrew Rabinovich. Atlas: End-to-end 3d scene reconstruction from posed images. In *ECCV*, 2020. 2, 3, 5
- [28] Maxime Oquab, Timothée Darcet, Théo Moutakanni, Huy Vo, Marc Szafraniec, Vasil Khalidov, Pierre Fernandez, Daniel Haziza, Francisco Massa, Alaaeldin El-Nouby, et al. Dinov2: Learning robust visual features without supervision. *arXiv preprint arXiv:2304.07193*, 2023. 2, 4
- [29] Guansong Pang, Chunhua Shen, Longbing Cao, and Anton Van Den Hengel. Deep learning for anomaly detection: A review. In *ACM Computing Surveys*, 2021. 1
- [30] Alec Radford, Jong Wook Kim, Chris Hallacy, Aditya Ramesh, Gabriel Goh, Sandhini Agarwal, Girish Sastry, Amanda Askell, Pamela Mishkin, Jack Clark, et al. Learning transferable visual models from natural language supervision. In *ICML*, 2021. 2
- [31] Lukas Ruff, Robert Vandermeulen, Nico Goernitz, Lucas Deecke, Shoaib Ahmed Siddiqui, Alexander Binder, Emmanuel Müller, and Marius Kloft. Deep one-class classification. In *ICML*, 2018. 1, 2

- [32] Danila Rukhovich, Anna Vorontsova, and Anton Konushin. Imvoxelnet: Image to voxels projection for monocular and multi-view general-purpose 3d object detection. In *WACV*, 2022. 2, 6
- [33] Johannes Lutz Schönberger, Enliang Zheng, Marc Pollefeys, and Jan-Michael Frahm. Pixelwise view selection for unstructured multi-view stereo. In *ECCV*, 2016. 6
- [34] Silvia Sellán, Jack Luong, Leticia Mattos Da Silva, Aravind Ramakrishnan, Yuchuan Yang, and Alec Jacobson. Breaking good: Fracture modes for realtime destruction. In *ACM Transactions on Graphics*, 2023. 5
- [35] Xuepeng Shi, Qi Ye, Xiaozhi Chen, Chuangrong Chen, Zhixiang Chen, and Tae-Kyun Kim. Geometry-based distance decomposition for monocular 3d object detection. In *ICCV*, 2021. 2
- [36] Stefan Stojanov, Anh Thai, and James M Rehg. Using shape to categorize: Low-shot learning with an explicit shape bias. In *CVPR*, 2021. 5
- [37] Jiaming Sun, Yiming Xie, Linghao Chen, Xiaowei Zhou, and Hujun Bao. Neuralrecon: Real-time coherent 3d reconstruction from monocular video. In *CVPR*, 2021. 2, 3
- [38] Blender Development Team. Blender (version 3.1.0) [computer software]. <https://blender.org/>, 2022. 5
- [39] Alex Trevithick and Bo Yang. Grf: Learning a general radiance field for 3d scene representation and rendering. In *ICCV*, 2021. 2
- [40] Vadim Tschernezki, Iro Laina, Diane Larlus, and Andrea Vedaldi. Neural feature fusion fields: 3d distillation of self-supervised 2d image representations. In *3DV*, 2022. 2
- [41] Qianqian Wang, Zhicheng Wang, Kyle Genova, Pratul P Srinivasan, Howard Zhou, Jonathan T Barron, Ricardo Martin-Brualla, Noah Snavely, and Thomas Funkhouser. Ibrnet: Learning multi-view image-based rendering. In *CVPR*, 2021. 2
- [42] Yue Wang, Yongbin Sun, Ziwei Liu, Sanjay E Sarma, Michael M Bronstein, and Justin M Solomon. Dynamic graph cnn for learning on point clouds. In *ACM Transactions on Graphics*, 2019. 6
- [43] Yue Wang, Vitor Campagnolo Guizilini, Tianyuan Zhang, Yilun Wang, Hang Zhao, and Justin Solomon. Detr3d: 3d object detection from multi-view images via 3d-to-2d queries. In *CoRL*, 2022. 2, 6
- [44] Jhih-Ciang Wu, Ding-Jie Chen, Chiou-Shann Fuh, and Tyng-Luh Liu. Learning unsupervised metaformer for anomaly detection. In *ICCV*, 2021. 2
- [45] Enze Xie, Zhiding Yu, Daquan Zhou, Jonah Philion, Anima Anandkumar, Sanja Fidler, Ping Luo, and Jose M Alvarez. M<sup>2</sup>BEV: Multi-camera joint 3d detection and segmentation with unified birds-eye view representation. *arXiv preprint arXiv:2204.05088*, 2022. 2
- [46] Guoyang Xie, Jinbao Wang, Jiaqi Liu, Feng Zheng, and Yaochu Jin. Pushing the limits of fewshot anomaly detection in industry vision: Graphcore. *arXiv preprint arXiv:2301.12082*, 2023. 2
- [47] Tianwei Yin, Xingyi Zhou, and Philipp Krahenbuhl. Center-based 3d object detection and tracking. In *CVPR*, 2021. 2
- [48] Alex Yu, Vickie Ye, Matthew Tancik, and Angjoo Kanazawa. pixelnerf: Neural radiance fields from one or few images. In *CVPR*, 2021. 2
- [49] Weihao Yuan, Xiaodong Gu, Heng Li, Zilong Dong, and Siyu Zhu. 3d former: Monocular scene reconstruction with 3d sdf transformers. *arXiv preprint arXiv:2301.13510*, 2023. 2
- [50] Junyi Zhang, Charles Herrmann, Junhwa Hur, Luisa Polania Cabrera, Varun Jampani, Deqing Sun, and Ming-Hsuan Yang. A tale of two features: Stable diffusion complements dino for zero-shot semantic correspondence. In *NeurIPS*, 2024. 2
- [51] Qiang Zhou, Weize Li, Lihan Jiang, Guoliang Wang, Guyue Zhou, Shanghang Zhang, and Hao Zhao. Pad: A dataset and benchmark for pose-agnostic anomaly detection. In *NeurIPS*, 2024. 2
- [52] Yang Zou, Jongheon Jeong, Latha Pemula, Dongqing Zhang, and Onkar Dabeer. Spot-the-difference self-supervised pre-training for anomaly detection and segmentation. In *ECCV*, 2022. 2